

Diffusion- and velocity-driven spatial separation of analytes from single droplets entering an ICP off-axis†

Cite this: *J. Anal. At. Spectrom.*, 2014, 29, 262

Olga Borovinskaya,^a Maryam Aghaei,^c Luca Flamigni,^a Bodo Hattendorf,^a Martin Tanner,^b Annemie Bogaerts^c and Detlef Günther^{*a}

The reproducible temporal separation of ion signals generated from a single multi-element droplet, observed in previous studies, was investigated in detail in this work using an ICPTOFMS with high temporal resolution. It was shown that the signal peak intensities of individual elements temporally shift relative to each other only for droplets moving through the plasma off-axis. The magnitude of these shifts correlated with the vaporization temperatures of the analytes and depended on the radial position of the droplets as well as on the thermal properties and velocity profiles of the carrier gases of the ICP. The occurrence of the signal shifting was explained by a spatial separation of analytes already present in the vapor phase in the ICP from a yet unvaporized residue of the droplet. This separation is most likely driven by anisotropic diffusion of vaporized analytes towards the plasma axis and a radial velocity gradient. The proposed explanation is supported by modeling of the gas velocities inside the ICP and imaging of the atomic and ionic emissions produced from single droplets, whose patterns were sloping towards the center of the torch. The effects observed in these studies are important not only for the fundamental understanding of analyte–plasma interactions but have also a direct impact on the signal intensities and stability.

Received 20th September 2013
Accepted 1st November 2013

DOI: 10.1039/c3ja50307k

www.rsc.org/jaas

1 Introduction

The dependence of the analyte response on the processes of sample-specific desolvation, vaporization, atomization, ion production and ion sampling in inductively coupled plasma mass spectrometry (ICPMS) has been extensively studied.^{2–8} Comprehensive understanding of these processes is a key to the accuracy of the chemical analysis. Common experimental approaches are based on continuous sample introduction and time-integrated measurements that make an assessment of the contribution of individual processes difficult.

The development of a monodisperse dried microparticulate injector (MDMI) by French,⁹ which allows well-defined discrete sample introduction, has opened the opportunity to follow these individual processes tracking single droplets/particles inside the ICP. Olesik *et al.* have used the MDMI for the first time to study the dependence of analyte vaporization on the

droplet size and plasma operating conditions.¹⁰ Later MDMI has been employed to investigate the processes of solvent evaporation, analyte vaporization and diffusion by means of time-resolved emission, laser induced fluorescence and mass spectrometry.^{11–13} Farnsworth and Lazar have conducted several studies to reveal the effect of different matrices on atomization and ionization processes.^{14,15} Local effects of analyte atomization on the plasma,^{16,17} ion sampling through the MS interface¹⁸ and space charge effects in the ion optics^{19,20} have also been assessed using isolated discrete droplets. Studying analyte–plasma interactions on a single droplet/particle level is essential to extract fundamentally and practically valuable information about bulk plasma processes. At the same time, understanding local processes, which a particular droplet or particle is subjected to in the ICP, is an important prerequisite for improving the analysis of single entities such as single particles²¹ or single cells.²²

Recently, we described a prototype ICP time-of-flight mass spectrometer (ICPTOFMS) with a temporal resolution of 30 μs .¹ A microdroplet generator was employed to characterize its capabilities for the multi-element analysis of single particles.¹ In the course of these studies a reproducible temporal variability of the occurrence of ion signals of different elements generated from the same droplet was noticed. Ion signal maxima of some elements were shifted from others by tens of microseconds. More surprising, however, was the observation

^aETH Zurich, Department of Chemistry and Applied Biosciences, Laboratory of Inorganic Chemistry, Wolfgang-Pauli-Strasse 10, CH-8093 Zurich, Switzerland. E-mail: guenther@inorg.chem.ethz.ch; Fax: +41 44-633-1071; Tel: +41 44-632-4687

^bTofwerk AG, Uttigenstrasse 22, CH-3600 Thun, Switzerland

^cResearch group PLASMANT, Department of Chemistry, University of Antwerp, Universiteitsplein 1, B-2610 Wilrijk, Antwerp, Belgium

† Electronic supplementary information (ESI) available. See DOI: 10.1039/c3ja50307k

that even the MS signals of chemically similar elements (La, Ce, Tb, Ho) appeared to be separated in time. A similar signal separation has previously been seen only for isotopes of significantly different masses, such as Pb and Li or Mg, using a dual mass analyzer and was explained by space charge effects predominantly.²⁰ Such effects, however, are not a likely explanation for the observation made in our studies because there was no distinct correlation between the magnitude of signal shifts and the isotope mass. It is thus far more likely that time shifting of the signals generated from the same droplet is a result of spatial separation of the analytes inside the ICP.

The current study was designed to reveal the cause and the origin of the signal separation. The dependence of the temporal shifts, signal durations and intensities on the radial position of the droplets, thermal properties of the ICP and the velocity profile of the gases inside the ICP was investigated in this work.

2 Experimental

2.1 Time-resolved mass spectrometry

A detailed description of the prototype ICPTOFMS used for these studies has been reported.¹ The signals of single multi-element droplets were acquired with a time resolution of 30 μs . The operating conditions of the ICPTOFMS shown in Table 1 were typically used unless otherwise specified.

2.2 Optical imaging and image processing

A commercial ICP mass spectrometer (ELAN 6000, PerkinElmer/Sciex, Ontario, Canada) with the same plasma generator and vacuum interface as in the ICPTOFMS was used for optical imaging. Emissions were imaged side-on *via* a Czerny-Turner grating monochromator (Spex series 1000, Horiba Ltd, Japan) operated in open-slit 2D imaging mode onto an iCCD camera (Andor iStar, Andor Technology, UK). A detailed description of the optical imaging setup can be found in ref. 23. Individual droplets consisting of a 100 mg kg⁻¹ strontium nitrate solution were introduced at a frequency of 100 Hz. Atomic and ionic emissions of Sr from single droplets were captured with 1 ms exposure time at 460 nm and 408 nm, respectively. The processing of optical images was realized using Fiji, an open source software.²⁴ A slice of an image apart from the Sr emission originated from a droplet was assumed to represent the plasma background and was subtracted from the entire picture. Images at all wavelengths were taken with the same magnification and the scale of the image was calibrated using the shadow of the load coil from the ArI emission (696 nm). The images were cropped to the same region, which was centered for ionic and atomic emissions separately along the arbitrarily chosen emission clouds which appeared to be straight.

2.3 Single droplet introduction

The single droplet introduction system used in these studies is based on a commercial microdroplet dispenser head (MD-K-150 with control unit MD-E-201-H, Microdrop Technologies GmbH, Norderstedt, Germany) and an Ar-He gas adapter arranged horizontally.¹ He and Ar gas flow rates were typically 0.4 l min⁻¹

Table 1 Operating conditions of the ICPTOFMS

Parameter	Value
Rf-power	1400 W
Plasma gas flow rate	16 l min ⁻¹
Auxiliary gas flow rate	1.2 l min ⁻¹
Cylindrical lens	6 V
Sampling depth	9.5 mm
Injector diameter	2 mm
Ar carrier gas flow rate	1.2 ^a l min ⁻¹
He carrier gas flow rate	0.4 ^a l min ⁻¹

^a Typical adjusted gas flow rates, varied in the course of some experiments.

and 1.2 l min⁻¹, respectively, unless otherwise specified. Droplets used for optical imaging were transported using a vertical assembly, consisting of a similar Ar-He gas adapter and a steel tube with an inner diameter of 4 mm.²⁵ An additional flow of Ar was admixed at the injector inlet to transport the droplets further into the ICP. The gas flow rates of He, Ar and the additional Ar were 0.4 l min⁻¹, 0.3 l min⁻¹ and 0.7 l min⁻¹, respectively. A schematic representation as well as specific characteristics of both single droplet transport systems can be found in ref. 26.

2.4 Materials

Multi-element solutions were prepared from single element standard solutions (Merck AG, Darmstadt, Germany and Inorganic Ventures, Christiansburg, Virginia, USA) diluting them to the required concentrations with 2% sub-boiled HNO₃ in ultra high purity (UHP) water (Millipore, Billerica, MA, USA). The solutions contained nitrate salts of Cu, Zn, Y, Cd, In, Ba, La, Ce, Ho, Er, Pb, and Bi. A suspension of the same CeO₂ nanoparticles (size range of 10–100 nm) as in ref. 26 was used. The suspension was sonicated for 15 min and diluted by a factor of 3000 with UHP water, then by a factor of 200 with a solution containing nitrates of Y and Bi. The concentrations of the solutions used are given for every experiment in the Results section.

2.5 Data evaluation

The size of the generated droplets was evaluated from the images taken with a CCD camera and the transient signals of the droplets were recorded by the data acquisition system of the ICPTOFMS. The details of data processing can be found in ref. 1. The temporal shifts of the signals shown here represent the time shifts of the respective intensity maxima from the maximum of the ⁸⁹Y⁺ signal (element with the earliest occurrence time) and is referred to as Δt :

$$\Delta t(E^+) = t(E^+) - t(^{89}\text{Y}^+)$$

where $\Delta t(E^+)$ is the time difference of the intensity maximum of an isotope E⁺ from the ⁸⁹Y⁺ intensity maximum of the signals originated from the same droplet.

The maxima positions and the full width at half maximum (FWHM) of the ICPTOFMS signals were found for each droplet

individually by performing the Gaussian fit. The maximum of the $^{89}\text{Y}^+$ signal was always used as the reference time (zero position) unless otherwise specified.

3 Results and discussion

3.1 Dependence of temporal shifts on droplet trajectories

In the course of these studies it was observed that the temporal shifts do not always occur and the magnitude of the shifts depends on operating parameters of the sample introduction system. Thus, both signals, with overlapping and with separated intensity maxima, were detected under certain operating conditions. An example of this situation can be seen in Fig. 1, where $^{165}\text{Ho}^+$ and $^{209}\text{Bi}^+$ signals of selected individual droplets of uniform size (the diameter evaluated from 140 shadowgraphy images was $41.0 \pm 0.4 \mu\text{m}$) are shown. Taking into account monodispersity of the generated droplets, it was assumed that the variability of temporal shifts likely arises from the instability of droplet trajectories.

In contrast to the example shown in Fig. 1, signals with reproducible temporal shifts could be attained after careful optimization of the carrier gas flow rates and the droplet size and its initial velocity by adjusting the actuator controlling voltage. Such transient signals of $40 \mu\text{m}$ droplets consisting of a 5 mg kg^{-1} Y, Ce and Bi solution are shown in Fig. 2. The shift of the $^{209}\text{Bi}^+$ signal relative to the $^{89}\text{Y}^+$ signal amounted to $115 \pm 10 \mu\text{s}$ (9% relative standard deviation (RSD), 500 droplets evaluated).

The magnitude of the shifts could be changed by rotating the dispenser head within the gas adapter. Fig. 3 shows how the shifts of the signal peaks could be increased by this rotation. As can be seen in Fig. 1 and 3, the signal duration (width) increases together with the magnitude of the temporal shift. Since all the remaining operating parameters were kept constant for both positions of the dispenser head, the change in the shifts can only arise from the change of the droplet trajectories in the transport system. Therefore, droplets followed two different paths at dispenser positions 1 and 2 (Fig. 3) and entered the plasma zone at different distances relative to the torch axis.

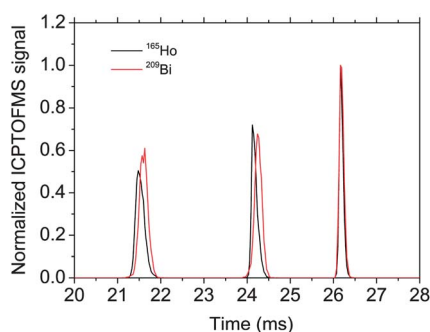


Fig. 1 Example of variability of the relative occurrence of maxima of $^{209}\text{Bi}^+$ and $^{165}\text{Ho}^+$ signals generated from individual droplets. The droplets consisted of a 10 mg kg^{-1} multi-element solution and had a diameter of $41.0 \pm 0.4 \mu\text{m}$, which was estimated by processing 140 video frames.

Despite significant signal broadening detected for position 2, there was no dramatic change in the integrated peak intensities of the isotopes studied. The In, Ba, La, Ce, Pb and Bi signals remained constant within less than 10% deviation. The ion signals of Y, Ho, Er, Cu, Zn and Cd, however, appeared to be less intense at position 2 (Fig. 3).

Fig. 2 shows data from an experiment where individual droplets (generated at 100 Hz) have a high variability of arrival times to the ICP. The temporal shifts of signal peaks from the maximum of the $^{89}\text{Y}^+$ signal and the element order within the corresponding signals, however, remained stable and their widths varied only slightly (the FWHM of 500 $^{209}\text{Bi}^+$ signals was $145 \pm 30 \mu\text{s}$). The residual size of the droplets has been found to depend on their trajectories and thus on the residence time in the transport system.²⁷ Our data indicate that the variation in

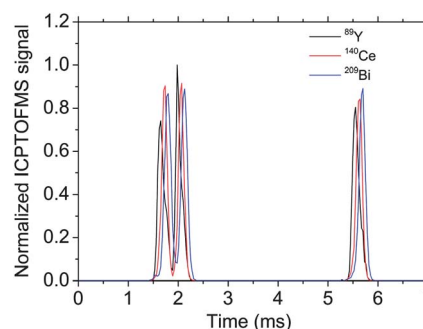


Fig. 2 Droplet signals with stable temporal shifts of $^{140}\text{Ce}^+$ and $^{209}\text{Bi}^+$ relative to the maximum of $^{89}\text{Y}^+$. This part of the measurement is chosen to illustrate a high temporal jitter in arrival times of the droplets into the plasma (droplets generated at 100 Hz). The droplets consisted of a 5 mg kg^{-1} Y, Ce and Bi nitrate solution and had a diameter of $39.0 \pm 0.4 \mu\text{m}$, which was estimated by processing 140 video frames.

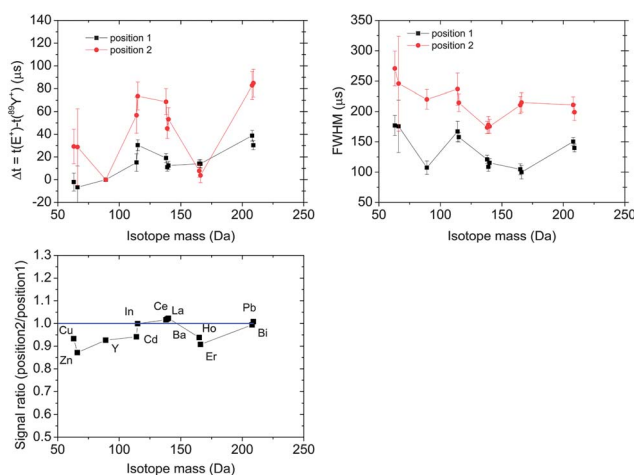


Fig. 3 Temporal shifts, FWHM of ICPTOFMS signals and ratios of signal intensities measured at two different positions. Position 2 was set by rotation of the dispenser head in the inlet of the transport assembly from position 1. The error bars of Δt and the FWHM represent 1 standard deviation (1 SD) of 1000 measurements of individual droplets. The line at signal ratio (position 2/position 1) = 1 and the lines between the points are drawn to guide the eye.

the residual droplet size caused by different delays of droplets in the transport system was not responsible for the temporal shifts.

To assess the degree of radial scatter of the droplet position in the plasma, imaging of the emission of atoms and ions produced from droplets consisting of a $\text{Sr}(\text{NO}_3)_2$ solution was carried out. Larger ($50\ \mu\text{m}$) droplets with a higher analyte concentration ($100\ \text{mg}\ \text{kg}^{-1}$) were used for this experiment to provide sufficient emission intensities. Therefore, the vertical droplet delivery system²⁶ had to be employed to ensure the transport of droplets into the ICP. For better contrast, the atomic emission was acquired at 1400 W ICP Rf-power and the ionic emission at 800 W. In contrast to the horizontal transport assembly, the variation of droplet trajectories in the vertical transport system is expected to be more pronounced due to the longer and bent transfer line. Fig. 4 depicts images of Sr atomic and ionic emission profiles generated from individual droplets taken with an exposure time of 1 ms. Profiles which start at an off-axis position show emission earlier that can be the result of a combination of the higher temperature at the boundary of the central channel and the longer path length of the droplet moving off-axis. Since excitation conditions depend on the local thermal properties of the ICP, the intensity of atomic or ionic emission alone does not represent the true analyte distribution in the plasma. However, the same sloping direction of clouds of ions and atoms is an indication of their continuous movement towards the sampler orifice.

Entrainment of an ion cloud into the sampler has previously been observed as far as 7 mm upstream from the orifice, being more pronounced 3 mm apart.¹⁸ That study has demonstrated that displacing the sampler orifice by 3 mm from the torch axis led to bending of Sr ion emission clouds. However, in our work, the sampler orifice position was in line with the injector tube while some of the droplets entered the plasma with radial offset. A bending of the Sr atom or ion emissions could be observed already $\approx 10\ \text{mm}$ away from the sampler orifice.

3.2 Dependence of temporal shifts and signal widths on plasma thermal properties

Δt was independent of the concentration of analytes in the droplet, whereas the signal width increased together with the peak integrated intensity (for more details see the ESI†).

The shifts and signal durations were strongly influenced by plasma operating conditions. The flow rate of He gas, which is supplied through the dispenser head, could be varied only in a narrow range of $0.2\text{--}0.6\ \text{l}\ \text{min}^{-1}$ to ensure stable operating conditions. Its effect on Δt , signal widths and intensities is shown in Fig. 5 for selected isotopes. The FWHM and temporal shifts decrease with increasing the He gas flow rate. The signal intensities follow the same trend with a less pronounced decrease for $^{209}\text{Bi}^+$. Assuming that the radial position of the droplets is not affected, the change of the FWHM can be explained by the penetration depth of the droplets inside the plasma. At higher gas flow rates the vaporization of a residue that remained after solvent evaporation will start deeper in the plasma. This will reduce the time available for the analyte vapor diffusion and result in smaller ion clouds at the sampling position and thus shorter signals. The suppression of signal intensities with the flow rate of He indicates either incomplete vaporization of the desolvated droplet residue and/or its lower ionization efficiency due to the higher fraction of He. In contrast to the flow rate of He, Δt changed randomly when the Ar gas flow rate was varied; this suggests that the droplet trajectories were affected.

To investigate the effect of ICP Rf-power, the flow rates of the carrier gases, He and Ar, were set to $0.4\ \text{l}\ \text{min}^{-1}$ and $1.3\ \text{l}\ \text{min}^{-1}$, where large temporal shifts between the peak signal of $^{89}\text{Y}^+$ and other elements could be reproducibly observed. Fig. 6 shows that Δt of the $^{209}\text{Bi}^+$ signal and the FWHM decrease with decrease of the plasma power. Lower plasma gas temperature at lower powers should shift the vaporization onset deeper inside the plasma and slow down diffusion in general, resulting in narrower MS signals, in a similar way to increasing the gas flow rates. However, the axial gas velocity will decrease with the Rf-power as well, increasing the residence time of the droplet and its vaporization products in the plasma before they reach the sampler. Therefore, only a slight effect on the FWHM was observed for refractory elements, which was even less pronounced for volatile elements, as Bi (Fig. 6). The same behavior of the FWHM with the change of the plasma power was also observed for signals whose maxima overlap (droplets moving on the plasma axis). It has been previously demonstrated that the position of complete vaporization of a single particle in the plasma shifts much less with the Rf-power than with the carrier gas flow rate.³ Nevertheless, it should be mentioned that the FWHM of MS signals is not a direct

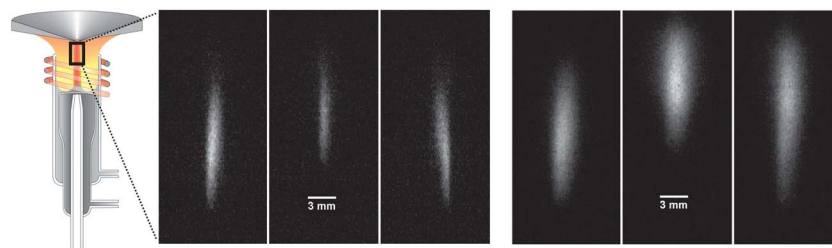


Fig. 4 Left: images of SrI emission produced from individual droplets acquired at 1400 W plasma power. Right: images of SrII emission produced from individual droplets recorded at a plasma power of 800 W for better contrast. An approximate position of the emission images in the plasma is indicated on the sketch shown in the left panel.

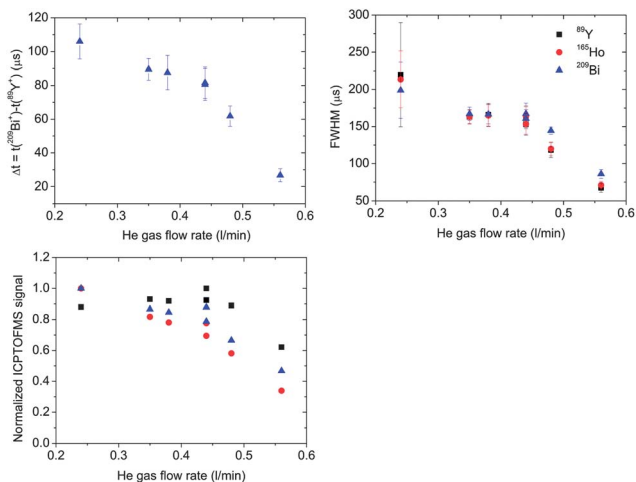


Fig. 5 Temporal shifts of the $^{209}\text{Bi}^+$ signal, FWHM and the normalized ICPTOFMS signal intensities of 3 isotopes measured at different He gas flow rates. The measurements at a gas flow rate of 0.44 l min^{-1} were conducted in the beginning and at the end of the experiment. The error bars represent 1 SD of 500 measurements of individual droplets.

representation of the ion cloud size but is also influenced by ion sampling and transport, which may not be the same at different plasma powers.⁸

Fig. 7 shows the dependence of Δt , FWHM and signal intensities on the flow rate of the auxiliary gas measured at the carrier gas flow rates mentioned above and 1400 W Rf-power. Even though the plasma central channel is expected to be hotter, which would increase the diffusion rate, a decrease of signal width was observed when reducing the auxiliary gas flow rate. Δt of the $^{209}\text{Bi}^+$ signal changes in the same way as the signal width (Fig. 7). The observed dependences indicate a link between signal widths and temporal shifts.

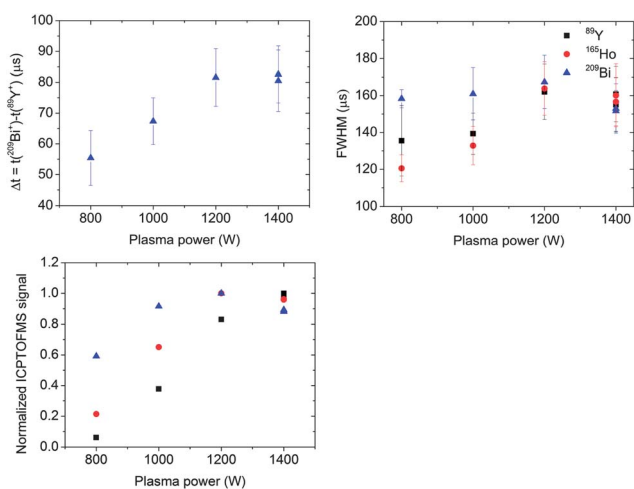


Fig. 6 Temporal shifts of the $^{209}\text{Bi}^+$ signal, FWHM and the normalized ICPTOFMS signal intensities of 3 isotopes measured at different plasma powers. The measurements at a plasma power of 1400 W were conducted in the beginning and at the end of the experiment. The error bars represent 1 SD of 500 measurements of individual droplets.

3.3 Element dependence of temporal shifts

Despite the variability observed in the magnitude of signal shifts, the sequence of occurrence of elements remained relatively constant in these experiments. For instance, the peaks of Y, Ce and Bi signals appear in this order when present in a solution containing 12 dissolved metals or only these three metals. As also shown previously,¹ the signal maxima of isotopes of the same element overlapped in time. Thus, if shifts occurred, the signal maximum of Y always appeared at the earliest time while the maxima of Bi and Pb were shifted most, irrespective of operating conditions.

Since the exact composition of the droplet residue formed inside the plasma after solvent evaporation is not known and thermal properties of the nitrate salts are often not available, the vaporization process of such a residue is difficult to describe. Therefore, the nitrates were assumed to decompose to oxides before volatilization. When plotting the temporal shifts against the reciprocal of boiling temperatures of the corresponding oxides (Fig. 8) a reasonable correlation can be seen, indicating that the vaporization process plays a dominant role in the temporal behavior of individual elements. Despite the scatter observed, Δt increases with decreasing oxide boiling temperatures. This suggests that the signal maxima of elements whose oxides start to vaporize earlier in the plasma have the longest delay.

To assess the validity of the assumed simplification, Δt of Ce signals generated from the droplets was compared for the dissolved nitrate salt and suspended oxide nanoparticles. Droplets consisting of a solution of $\text{Y}(\text{NO}_3)_3$ and $\text{Bi}(\text{NO}_3)_3$ at concentrations of 5 mg kg^{-1} together with either $\text{Ce}(\text{NO}_3)_3$ at the same concentration or a suspension of CeO_2 nanoparticles in a size range between 10 nm and 100 nm were measured. To provide an adequate signal intensity, the initial suspension was diluted in a way that more than 1 particle was present per droplet. A

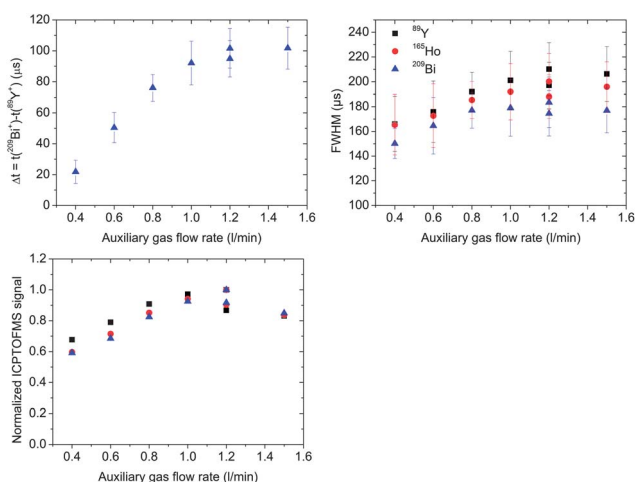


Fig. 7 Temporal shifts of the $^{209}\text{Bi}^+$ signal, FWHM and the normalized ICPTOFMS signal intensities of 3 isotopes measured at different auxiliary gas flow rates. The measurements at a gas flow rate of 1.2 l min^{-1} were conducted in the beginning and at the end of the experiment. The error bars represent 1 SD of 500 measurements of individual droplets.

comparison of the temporal shift of Ce relative to Y for the different species is shown in Fig. 9. The reproducibility of the Bi shift indicates that the measurement conditions remained stable for both species. Despite the larger spread, the occurrence of the signal maxima of both Ce isotopes did not show a distinguishable difference for CeO₂ nanoparticles compared to dissolved Ce(NO₃)₃.

3.4 Inverse element order of temporal shifts with 0.85 mm injector diameter

Droplets consisting of a solution containing Y, Ce, Hf, Bi and Th were measured using injectors with 2 mm and 0.85 mm diameters. The carrier gas flow rates and dispenser parameters had to be optimized for both injectors separately to attain maximally stable Δt , whereas the plasma power and auxiliary gas flow rate were kept constant (Table 1). In contrast to the wider injector, where the signal maxima of Hf isotopes appeared first and Bi showed the longest delay, the order was reversed and the ²⁰⁹Bi⁺ signal occurred at the earliest time when using the injector with the smaller diameter. Reference time positions of signals of a single droplet were set on the maxima of the ¹⁷⁸Hf⁺ and ²⁰⁹Bi⁺ signals for the 2 mm and 0.85 mm injector diameters, respectively. The temporal shifts of other isotopes from these reference positions are given in Table 2. Δt determined for the 0.85 mm injector were smaller and the signals much narrower, most likely because the vaporization onset was shifted further downstream in the plasma by the higher carrier gas initial velocity. The signal maxima of Hf and Th, whose oxides have the highest boiling points (5673 K and 4673 K) of all elements investigated, overlapped for the 0.85 mm injector but Δt of other isotopes follow an inverse order. It is important to mention that whenever shifts occurred, the element order with the 0.85 mm injector was always reverse of that observed with the 2 mm injector irrespective of operating conditions, droplet size and its initial velocity.

3.5 Interpretation of temporal shifts

For the signal maxima of elements to be temporally separated by 100 μ s the center of mass of the corresponding ion clouds

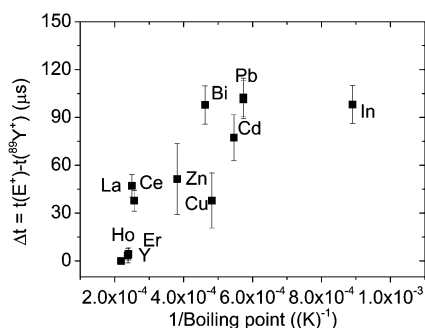


Fig. 8 Temporal shifts of all elements (except Ba) present in the multi-element solution plotted against the reciprocal of boiling points of the corresponding oxides (see the ESI†). The carrier gas flow rates of He and Ar were 0.4 l min⁻¹ and 1.3 l min⁻¹, respectively. The error bars represent 1 SD of 500 measurements of individual droplets.

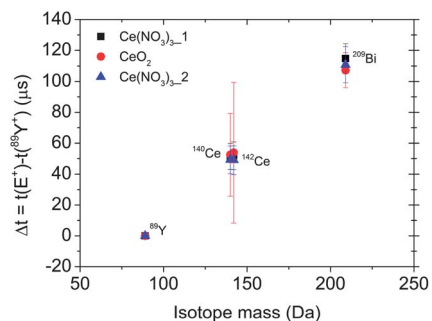


Fig. 9 Temporal shifts of ²⁰⁹Bi⁺, ¹⁴⁰Ce⁺, ¹⁴²Ce⁺ ICPTOFMS signals from the signal of ⁸⁹Y⁺ (shown at $\Delta t = 0$ on the graph) measured with droplets consisting of a Y, Ce and Bi nitrate solution and a solution of Y and Bi nitrate containing CeO₂ nanoparticles. Δt for Ce(NO₃)₃ was measured twice, before and after the measurement of Δt for CeO₂.

would have to be separated along the axis of the ICP by 2 mm, assuming an average gas velocity of 20 m s⁻¹.²⁸ Such a significant spatial separation might occur if elements are distributed in different discrete phases formed from a multi-element droplet.

Garcia *et al.* have observed element phase separation in individual aqueous droplets desolvated at elevated temperatures (200 °C) and formation of particles of different element compositions, morphologies and sizes.²⁹ Particles of different sizes and masses might attain different velocities in the plasma due to the drag force of the accelerating gas and, as a result, ions generated from smaller particles should be sampled and detected earlier. In the same way the vapor phase generated from a particle could be accelerated in relation to the particle itself. However, this effect would be the same for both droplets moving on- and off-axis. The element sequence of signals and its reproducibility strongly indicate that this effect is most likely not responsible for the signal shifting. Nevertheless, elemental inhomogeneity of a residue produced in the plasma after solvent evaporation, formation of a layer like structure or even different particles cannot be excluded.

The experimental observations suggest that the temporal shifting of the signals is a result of an element fractionation in

Table 2 Temporal shifts of ICPTOFMS signals from the reference position (shown as dash) generated from a single droplet measured with 2 mm and 0.85 mm injector diameters. The values are given in μ s. The carrier gas flow rates of He and Ar and the droplet size for the 0.85 mm injector diameter were 0.3 l min⁻¹ and 0.7 l min⁻¹, and 37.0 \pm 0.3 μ m, respectively, and the corresponding values for the 2 mm injector diameter were 0.4 l min⁻¹ and 1.1 l min⁻¹, and 32.0 \pm 0.3 μ m, respectively. The plasma power, plasma gas and auxiliary gas flow rates remained constant for both experiments. The errors represent 1 SD of 500 measurements of individual droplets

Isotope	Δt (2 mm)	Δt (0.85 mm)
⁸⁹ Y	42 \pm 16	35 \pm 19
¹⁴⁰ Ce	153 \pm 32	28 \pm 9
¹⁷⁸ Hf	—	57 \pm 22
²⁰⁹ Bi	184 \pm 57	—
²³² Th	55 \pm 15	59 \pm 19

the plasma, which is directly related to vaporization and diffusion. These processes strongly depend on the local plasma conditions, which differ for droplets moving on- and off-axis. As discussed, droplets at the outer boundaries of the central channel probably start to evaporate and the desolvated residue to vaporize earlier thanks to the hotter plasma in this region. The species produced during vaporization will undergo diffusion-driven expansion, which is proportional to the plasma gas temperature and the atomic mass of an analyte.³ A decrease of the widths of emission clouds and MS signals with an increase of the atomic mass of the analyte has been previously demonstrated.^{13,17} However, although the FWHM did show a general increase with decreasing isotope mass in these studies, that effect was clearly overprinted by the chemical properties of the elements (Fig. 3). Signal broadening can be predominantly explained by an atomic mass dependence of the diffusion if vaporization onsets are located at the same position for all elements and the distortion of ion clouds in the ion optics is excluded. The broad range of vaporization temperatures of the analytes (considering oxides of the corresponding elements) used in this work might also be responsible for the deviation of our results from the expected behavior.

Diffusion as an isotropic process, generating a symmetrical ion distribution, can only occur for very small clouds.¹⁷ This may be true if an analyte moves on the central axis of the torch, where the temperature gradient remains comparably small. With displacement of its trajectory from the plasma axis the uniformity of vapor expansion might be distorted. In this case the diffusion rate can increase in one direction due to gradients of temperature, gas density or plasma viscosity.

The vertical profiles of the Sr atomic and ionic emissions shown in Fig. 4 indicate a continuous movement of the analyte cloud towards the central axis of the torch when the droplets enter the ICP off-axis. This movement could be caused by the gas entrainment into the sampler, as has been previously shown.¹⁸ However, the entrainment cannot explain the temporal shifts since the ion cloud would move in the same direction and at the same velocity as the particle it originates from. The shifts may, however, occur if the vaporized analyte moves towards the plasma axis due to the preferential diffusion in this direction. This behavior can probably be explained by a higher plasma viscosity at the outer region of the central gas channel, which would hinder the analyte expansion in this direction.³⁰

Thus, atoms and ions of the analytes which vaporize earlier in the plasma start to diffuse towards the plasma axis earlier than those of the refractory ones, which vaporize further downstream. For the spatial separation of elements to occur, the fraction of the gas on the central axis must have a different velocity from that at the boundaries. Gas acceleration due to the increase of the plasma gas temperature can be expected with the radial distance, especially approaching the zone of the highest power coupling.³⁰ Therefore, in the case of the 2 mm injector diameter, the gas velocity most likely decreases towards the plasma axis, causing a continuous delay of the vapor phase in this region (enriched in volatile elements) from the particle residue (enriched in refractory elements). Reducing the injector

diameter to 0.85 mm leads to a significant increase of the initial velocity of the carrier gas.⁴ However, the gas velocities at the outer boundaries of the central channel were probably similar for both injectors, being determined by the same auxiliary gas flow and plasma power (Table 1). Thus, for droplets which are close to the outer boundaries, the inverse velocity gradient can cause an acceleration of the volatile species in relation to the refractory ones. Therefore, the order in which signal maxima of elements appeared can be explained by a vaporization sequence of the corresponding analytes from the desolvated residue of the droplet and the direction of the radial velocity gradient.

The experimentally observed dependences of temporal shifts on the plasma operating conditions are consistent with the proposed explanation. An increase of the injector gas flow rate increases the penetration depth of the droplet and reduces its residence time in the plasma that is consistent with less pronounced signal shifts and widths. Moreover, at a higher rate of the injector gas flow the difference of gas velocities between the plasma axis and the central channel boundaries might be reduced, which additionally should reduce Δt . Smaller shifts were also detected at lower plasma powers, which can further be related to the delay of the vaporization onset of the desolvated residue within the plasma and the smaller radial velocity gradient. Additionally, the diffusion rate will likely be lower when operating at low plasma powers and high injector gas flow rates, which will also reduce the Δt , as outlined in Section 3.2. The decrease of Δt with the decrease in the auxiliary gas flow rate, which at first glance seems to be contradicting, can probably be explained by a less steep radial velocity gradient established due to a better energy exchange between the central channel and the outer region of the plasma.

The behavior of the signal integrated intensities with the change of the droplet radial position, shown in Section 3.1, can also be explained by the suggested hypothesis. The In, Ba, La, Ce, Pb and Bi signals, which peak with the longest delay, remained constant. This indicates that the ions of these elements can be efficiently sampled due to the effect of diffusion-driven focusing even if the initial position of the droplet was shifted from the plasma axis. Y, Ho and Er most likely penetrate deeper into the plasma due to their higher vaporization temperatures, thus following the outer streamline for a longer period of time. Therefore, a part of these analytes might still be present off-axis at the sampler position. The decrease of their signal intensities can be explained either by an incomplete entrainment of the ion cloud or a drop in ion density due to the cooling effect at the sampler surface. The signal suppression of Cu, Zn and Cd can only partially be assigned to the same process, since they were still detected with longer delays than Y, Ho and Er. The oxides of Cu, Zn and Cd are of similar volatility (2073 K, 2623 K and 1832 K, respectively) and have lower atomic masses than the other elements. Thus, the rest of the ion loss can probably be explained by an increased rate of the overall diffusion with the radial shift of the droplet to a hotter region in the plasma. The overall relative invariability of signal intensities with the radial distance of the droplets suggests that the above described processes must take place within the region of the central gas flow. Even though the signal suppression is

discussed only from the perspective of vaporization and diffusion, the processes of excitation and ionization might also change along the radial distance in the ICP.

3.6 Plasma gas velocity modeling

To verify the proposed hypothesis the gas velocities inside the ICP were calculated using FLUENT, a commercial computational fluid dynamics (CFD) program, which was already employed in several theoretical studies.^{30–33} The operating conditions used for the simulation were matched as closely as possible with the experiments where the maximal temporal shifts were detected and are shown in Table 3. The velocities were calculated only for the 2 mm injector diameter. A more detailed description of the model can be found in ref. 30–33.

The positions of three streamlines of the injector gas in the torch and their scalar velocities are shown in Fig. 10a and b for an auxiliary gas flow rate of 1.2 l min⁻¹, respectively. The fraction of the gas closer to the highest power coupling region (represented with the green line in Fig. 10b) accelerates earlier due to the increase of the gas temperature and reaches a higher velocity than the central streamline (represented by the black line) along the distance from the second turn of the induction coil until short before the MS-interface. A few millimeters away from the sampler cone orifice the velocities rise steeply due to the gas entrainment through the sampler cone. The part of the gas close to the cooled metal surface of the sampler cone decelerates before the entrainment. Thus, if a desolvated droplet residue travels off-axis with the local gas velocity (green line in Fig. 10b) its vaporized part diffusing towards the plasma axis can be continuously delayed from the yet unvaporized residue along a distance of more than 10 mm. The same simulation was performed for an auxiliary gas flow rate of 0.4 l min⁻¹. As shown in Fig. 10c, the relative difference in scalar velocities between the central and the outer streamlines is reduced in comparison with the flow rate of 1.2 l min⁻¹, which can explain the experimentally observed decrease of the magnitude of the temporal shifts.

The radial component of the velocities of the streamlines calculated with an auxiliary gas flow rate of 1.2 l min⁻¹ is plotted in Fig. 10d. This pattern indicates hindering of the radial gas expansion in the region close to the highest plasma coupling (approximately between 15 mm and 30 mm), probably by a higher viscosity of the core plasma. Furthermore, there is no gas

movement directed towards the center of the torch, suggesting that only anisotropic diffusion can lead to the observed bending of the atom and ion clouds (Fig. 4) towards the axis of the ICP until only short before entering the sampler orifice.

3.7 Analytical consequences

The dependence of the detection efficiency of a single droplet/particle on its radial position in the plasma has already been discussed.³⁴ If discrete samples are introduced into the plasma in a random manner, a scatter in their radial position will be an additional source of error and can deteriorate the quality of their analysis. In the course of these studies it was shown that signal intensities of the elements which start to vaporize earlier in the plasma are not affected by the radial shift of the droplets from the central axis, probably due to the effect of the inward diffusion. Therefore, if the right operating conditions are chosen, this effect might play a role of self-focusing of analyte clouds generated from single particles off-axis in the plasma improving the precision of nanoparticle size determination. However, signals of some elements, including REEs, could be suppressed by as much as 10% if droplets move off-axis. Since REEs are used for labeling and detection of single cells, this observation will be of particular importance for example in mass cytometry. The effect of the radial scatter on the detection efficiency of single particles and cells has to be investigated in more detail; nevertheless, a proper sample focusing in the plasma will most likely improve the analysis precision. Nebulizer/spray chamber sample introduction systems, which generate polydisperse aerosols, are definitely more robust and convenient to use in comparison to the single droplet introduction. However, for certain applications such as the analysis of small aliquots of precious liquids and single particle/cell mass quantification, the nebulizer/spray chamber system might not be the most suitable.

If the radial location of droplets entering the ICP can be controlled precisely and a steeper velocity gradient can be achieved, the observed effect of the analyte-specific element fractionation in combination with high speed multi-element signal acquisition could be employed to resolve isobaric interferences. An important requirement for an effective element separation in the plasma would be significantly different vaporization temperatures. In fact, the separation of the maxima of ⁸⁷Rb and ⁸⁷Sr signals was already observed in our laboratory for nitrate salts using the same setup (Fig. 11). The potential of this approach must, however, be evaluated based on a detailed study.

Table 3 Plasma operating and boundary conditions used in the model for calculating the gas velocities inside the ICP

Parameter	Value
Injector gas flow rate (He and Ar)	0.4 and 1.2 l min ⁻¹
Auxiliary gas flow rate	1.2 l min ⁻¹
Plasma gas flow rate	16 l min ⁻¹
Rf-frequency	27 MHz
Input Rf-power	1400 W
Inlet gas temperature	297 K
Sampler cone temperature	500 K
Pressure at the sampler cone	134 Pa
Sampling depth	9.5 mm

4 Conclusions

The element-dependent temporal shifts of ICPMS signals generated from an individual droplet consisting of a multi-element solution were studied in detail by optical emission imaging and time-resolved mass spectrometry. It was proposed that the temporal separation of signal peaks can occur only for droplets moving in the plasma with a radial shift from the central axis.

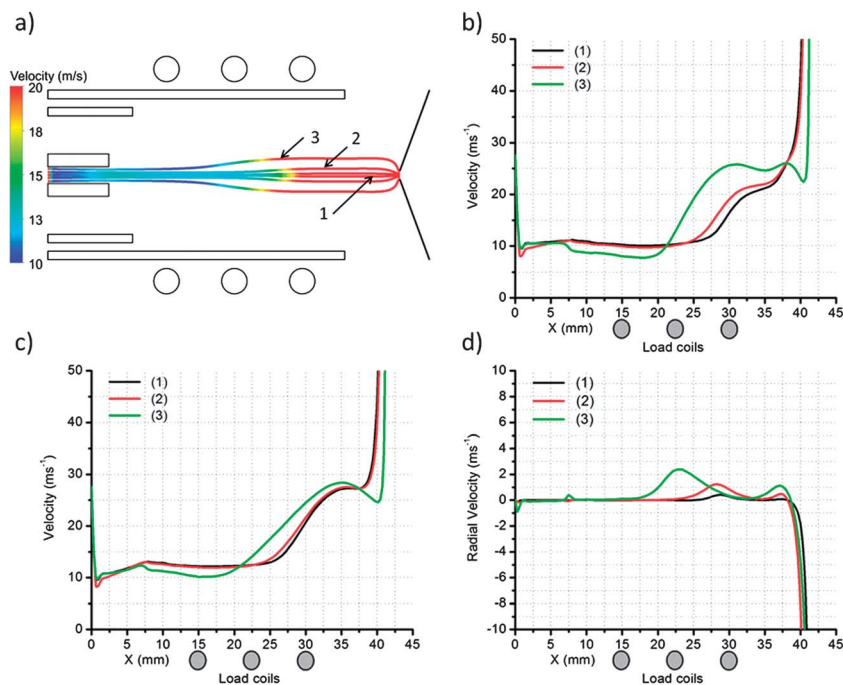


Fig. 10 (a) Scalar velocities and paths of three streamlines originating from the injector gas. (b) Scalar velocities of three streamlines as a function of the axial distance from the injector inlet calculated with an auxiliary gas flow rate of 1.2 l min^{-1} . The black curve represents the streamline at the central axis, the green curve is the outermost streamline and the red one is a streamline in between. (c) Scalar velocities calculated with an auxiliary gas flow rate of 0.4 l min^{-1} . (d) Radial component of the velocities of the streamlines shown in (a) and (b).

The magnitude of this separation as well as the FWHM of the signals varied with the droplet radial position and thermal properties of the ICP. Based on the experimental results and modeling of the gas velocities inside the ICP it was concluded that droplets which follow off-center trajectories in the plasma are subjected to an analyte-dependent spatial element fractionation, which causes the temporal separation of signal maxima. This element fractionation takes place *via* anisotropic diffusion of vaporized analytes towards the plasma axis where the radial velocity gradient continuously separates them in space from the still unvaporized droplet residue. Thus, if the velocity increases with the radial distance from the plasma axis, the volatile species, which vaporize earlier in the plasma, will be delayed from the analytes with higher boiling temperatures. As a result of this delay, the signals of the most volatile elements

are detected with the highest temporal shifts from the most refractory elements. *Vice versa*, the volatile species will be accelerated and their signals will be detected before the refractory ones if the velocity gradient has an inverse direction. Therefore, the element order of the occurrence of signals generated from a multi-element droplet is defined by vaporization temperatures of the corresponding analytes and the direction of the radial velocity gradient of the plasma, whereas the magnitude of the signal shifts is determined by the radial position of the droplets and thermal properties of the ICP.

Acknowledgements

Financial support by the KTI (project number: 10804.2 PFNM-NM) and ETH Zürich (project number: ETH-49 12-2) is gratefully acknowledged. The authors would like to thank Jörg Meili and Hao Wang for their help in developing the codes for data evaluation, Joachim Koch for useful discussions and Marc Gonin for reviewing this manuscript. Furthermore, financial support from the University of Antwerp through the Methusalem Financing is gratefully acknowledged. Finally, the authors would like to express their gratitude to two anonymous reviewers whose valuable comments improved the quality of this manuscript.

References

- O. Borovinskaya, B. Hattendorf, M. Tanner, S. Gschwind and D. Günther, *J. Anal. At. Spectrom.*, 2013, **28**, 226–233.

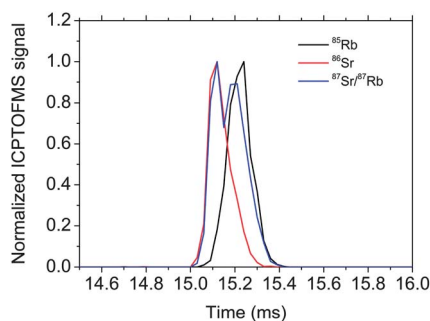


Fig. 11 Normalized ICPTOFMS signals generated from a droplet consisting of a 5 mg kg^{-1} Rb nitrate and 20 mg kg^{-1} Sr nitrate solution.

- 2 J. A. Horner, S. A. Lehn and G. M. Hieftje, *Spectrochim. Acta, Part B*, 2002, **57**, 1025–1042.
- 3 J. A. Horner and G. M. Hieftje, *Spectrochim. Acta, Part B*, 1998, **53**, 1235–1259.
- 4 L. Flamigni, J. Koch and D. Günther, *Spectrochim. Acta, Part B*, 2012, **76**, 70–76.
- 5 M. W. Blades and G. Horlick, *Spectrochim. Acta, Part B*, 1981, **36**, 861–880.
- 6 B. L. Caughlin and M. W. Blades, *Spectrochim. Acta, Part B*, 1985, **40**, 1539–1554.
- 7 S. E. Hobbs and J. W. Olesik, *Spectrochim. Acta, Part B*, 1993, **48**, 817–833.
- 8 J. H. Macedone, D. J. Gammon and P. B. Farnsworth, *Spectrochim. Acta, Part B*, 2001, **56**, 1687–1695.
- 9 J. B. French, B. Etkin and R. Jong, *Anal. Chem.*, 1994, **66**, 685–691.
- 10 J. W. Olesik and S. E. Hobbs, *Anal. Chem.*, 1994, **66**, 3371–3378.
- 11 J. W. Olesik, J. A. Kinzer and G. J. McGowan, *Appl. Spectrosc.*, 1997, **51**, 607–616.
- 12 J. W. Olesik, *Appl. Spectrosc.*, 1997, **51**, A158–A175.
- 13 M. P. Dziewatkoski, L. B. Daniels and J. W. Olesik, *Anal. Chem.*, 1996, **68**, 1101–1109.
- 14 A. C. Lazar and P. B. Farnsworth, *Appl. Spectrosc.*, 1999, **53**, 457–464.
- 15 A. C. Lazar and P. B. Farnsworth, *Appl. Spectrosc.*, 1999, **53**, 465–470.
- 16 S. Groh, C. C. Garcia, A. Murtazin, V. Horvatic and K. Niemax, *Spectrochim. Acta, Part B*, 2009, **64**, 247–254.
- 17 A. Murtazin, S. Groh and K. Niemax, *Spectrochim. Acta, Part B*, 2012, **67**, 3–16.
- 18 I. I. Stewart, C. E. Hensman and J. W. Olesik, *Appl. Spectrosc.*, 2000, **54**, 164–174.
- 19 J. Olesik and M. Dziewatkoski, *J. Am. Soc. Mass Spectrom.*, 1996, **7**, 362–367.
- 20 L. A. Allen, J. J. Leach and R. S. Houk, *Anal. Chem.*, 1997, **69**, 2384–2391.
- 21 C. Degueldre and P. Y. Favarger, *Colloids Surf., A*, 2003, **217**, 137–142.
- 22 S. C. Bendall, E. F. Simonds, P. Qiu, E.-A. D. Amir, P. O. Krutzik, R. Finck, R. V. Bruggner, R. Melamed, A. Trejo, O. I. Ornatsky, R. S. Balderas, S. K. Plevritis, K. Sachs, D. Pe'er, S. D. Tanner and G. P. Nolan, *Science*, 2011, **332**, 687–696.
- 23 L. Flamigni, J. Koch and D. Günther, *J. Anal. At. Spectrom.*, 2013, DOI: 10.1039/C3JA50314C.
- 24 J. Schindelin, I. Arganda-Carreras, E. Frise, V. Kaynig, M. Longair, T. Pietzsch, S. Preibisch, C. Rueden, S. Saalfeld, B. Schmid, J.-Y. Tinevez, D. J. White, V. Hartenstein, K. Eliceiri, P. Tomancak and A. Cardona, *Nat. Methods*, 2012, **9**, 676–682.
- 25 S. Gschwind, L. Flamigni, J. Koch, O. Borovinskaya, S. Groh, K. Niemax and D. Günther, *J. Anal. At. Spectrom.*, 2011, **26**, 1166.
- 26 S. Gschwind, H. Hagedorfer, D. A. Frick and D. Günther, *Anal. Chem.*, 2013, **85**, 5875–5883.
- 27 J. Koch, L. Flamigni, S. Gschwind, S. Allner, H. Longenrich and D. Günther, *J. Anal. At. Spectrom.*, 2013, **28**, 1707–1717.
- 28 L. Flamigni, J. Koch, H. Wiltsche, R. Brogioli, S. Gschwind and D. Günther, *J. Anal. At. Spectrom.*, 2012, **27**, 619–625.
- 29 C. C. Garcia, A. Murtazin, S. Groh, M. Becker and K. Niemax, *Spectrochim. Acta, Part B*, 2010, **65**, 80–85.
- 30 H. Lindner, A. Murtazin, S. Groh, K. Niemax and A. Bogaerts, *Anal. Chem.*, 2011, **83**, 9260–9266.
- 31 M. Aghaei, H. Lindner and A. Bogaerts, *J. Anal. At. Spectrom.*, 2012, **27**, 604–610.
- 32 M. Aghaei, H. Lindner and A. Bogaerts, *Spectrochim. Acta, Part B*, 2012, **76**, 56–64.
- 33 M. Aghaei, H. Lindner and A. Bogaerts, *J. Anal. At. Spectrom.*, 2013, **28**, 1485–1492.
- 34 J. W. Olesik and P. J. Gray, *J. Anal. At. Spectrom.*, 2012, **27**, 1143–1155.